Investigations of Temporal and Spatial Distribution of Precursors SO$_2$ and NO$_2$ Vertical Columns in North China Plain by Mobile DOAS

Fengcheng Wu[1], Pinhua Xie[1,3,4*], Ang Li[1], Fusheng Mou[1], Hao Chen[1], Yi Zhu[2], Tong Zhu[2], Jianguo Liu[1], Wenqing Liu[1]

[1] Key Laboratory of Environmental Optical and Technology, Anhui Institute of Optics and Fine Mechanics, Chinese Academy of Sciences, Hefei, 230031, China

[2] State Key Laboratory of Environmental Simulation and Pollution Control, College of Environmental Sciences and Engineering, Peking University, Beijing, 100871, China

[3] Center for Excellence in Regional Atmospheric Environment, Institute of Urban Environment, Chinese Academy of Sciences, Xiamen, 361021, China

[4] School of Environmental Science and Optoelectronic Technology, University of Science and Technology of China, Hefei, 230026, China

Correspondence to: P. H. Xie (phxie@aiofm.ac.cn)

Abstract: Recently, Chinese cities have suffered severe events of haze air pollution, particularly in the North China Plain (NCP). Investigating the temporal and spatial distribution of pollutants, emissions, and pollution transport is necessary to better understand the effect of various sources on air quality. We report on mobile differential optical absorption spectroscopy (mobile DOAS) observations of precursors SO$_2$ and NO$_2$ vertical columns in NCP in summer of 2013 (from 11 June to 7 July) in this study. The different temporal and spatial distributions of SO$_2$ and NO$_2$ vertical column density (VCD) over this area are characterized under various wind fields. The results show that the transport from southern NCP strongly affects the air quality in Beijing, and the transport route, particularly SO$_2$ transport of Shijiazhuang–Baoding–Beijing is identified. In addition, the major contributors to SO$_2$ along the route of Shijiazhuang–Baoding–Beijing are elevated sources and low area sources for the route of Dezhou–Cangzhou–Tianjin–Beijing are found using the interrelated analysis between in situ and mobile DOAS observations during the measurement periods. Furthermore, the discussion of hot spot near Ji'nan City shows that the average observed width of polluted air mass is 11.83 km and 17.23

Atmospheric
Chemistry
and Physics
Discussions

km associated with air mass diffusion, which is approximately 60 km away from emission sources based on geometrical estimation. Finally, a reasonable agreement exists between OMI and mobile DOAS observations with correlation coefficient (R^2) of 0.65 for NO_2 VCDs. Both datasets also have similar spatial pattern. The fitted slop of 0.55 is significantly less than unity can reflect the

5 contamination of local sources and OMI observations need to improve the sensitivities to the near-surface emission sources through the improvements of retrieval algorithm or resolution of satellites.

1. Introduction

10 Driven by the unprecedented economic growth and explosive increase in urbanization, China has been experiencing severe air pollution, particularly in developed areas, such as, Yangtze River Delta region and Pearl River Delta region (van Donkelaar et al., 2010). The severe haze pollution events occurred frequently since the end of 2012 in Jing-Jin-Ji region, including Beijing, Tianjin, Shijiazhuang, and some cities in Hebei province. Long duration, heavy pollution level, and large spread area are the main

15 characteristics of haze pollution, which have been rare in the past decades (Sun et al., 2014; Ji et al., 2014; Zhao et al., 2013). Haze pollution has affected the health and lifestyle of millions, drawing extensive worldwide attention on China. Severe air pollution in Beijing, the capital of China, has troubled the public, scholars, and the government. Concurrently, many studies have been conducted in Beijing and its surrounding areas (Wang et al., 2014a; Wang et al., 2014b; Xu et al., 2011; Ma et al.,

20 2012). Related results show that the air pollution in Beijing is a regional environmental problem caused by the influences of both local emission and external transport (Ying et al., 2014; Guo et al., 2014; Wu et al., 2011).

NO_2 is one of the most important atmospheric trace gases. It plays a key role in tropospheric and stratospheric chemistry and strongly participates in the chain reaction formation of tropospheric ozone

25 (Crutzen et al., 1970). Moreover, NO_2 is the main pathway of OH loss, which determines the atmospheric oxidative capacity, under heavy polluted conditions (Finlayson-Pitts et al., 1999; Kanaya et al., 2014). Aside from NO_2 being generally harmful to human health, long-term NO_2 exposure in high concentrations can also increase the possibility of bronchitis in asthmatic children (WHO, 2006). Combustion processes, such as power generation and release of pollutants from vehicles, are the major

30 sources of anthropogenic NO_2 emissions. Meanwhile, SO_2 is a colorless gas that adversely affects the

respiratory system. Emissions from elevated releases, such as that from power plants, are the main

contributor for anthropogenic SO_2 emission (Xu et al., 1998; Ramanathan et al., 2003). Furthermore,

NO_2 and SO_2 are important precursors of aerosol. Under suitable meteorological conditions, NO_2 and

SO_2 tend to form nitrate and sulfate, which contribute to the formation of secondary aerosols (Jang et

5   al., 2001; Boichu et al., 2015). Some studies show that nitrate and sulfate account for large proportions

in particulate matter ($PM_{2.5}$, with aerodynamic diameter less than or equal to 2.5μm), which is an

important element of haze, in Jing-Jin-Ji region (Huang et al., 2014; Yang et al., 2011, Sun et al., 2013,

Zhang et al., 2013). Based on model simulation, $PM_{2.5}$ concentration can be significantly reduced if

SO_2 and NO_x emission have been controlled effectively (Zhao et al., 2013). In addition, the spatial and

10   temporal distributions of SO_2 and NO_x vary significantly (Lee et al., 2009;Matsui et al., 2009; Wang et

al., 2009). To investigate the spatial and temporal distribution of SO_2 and NO_2 and evaluate the

influence of transport on Beijing the observations of distribution of tropospheric SO_2 and NO_2 vertical

column density (VCD) was conducted in North China Plain (NCP) using mobile DOAS from June to

July 2013. NCP is located in northern China, surrounded by Taihang Mountain (at the west of NCP),

15   Yanshan Mountain (at the north of NCP) and Bohai Sea (at the east of NCP). NCP consists of the

Jing-Jin-Ji region and other provinces in Northern China and is one of the heaviest polluted areas in

China (Quan et al., 2011).

A large number of studies on distributions of air pollutants have also been performed in NCP. The

characteristics of concentration and evolution at different sites and formation mechanisms during heavy

20   pollution periods have been researched using ground-based observation networks (Hu et al., 2014).

Meanwhile, regional variations of gas, particle pollutants, and other factors which influence pollution

characteristics have been detected using airborne measurement (Zhang et al., 2014). Also, based on

mobile laboratory, Wang et al. (2011) analyzed the regional distribution of SO_2 in Beijing and its

surrounding areas and estimated transport flux from the outside to Beijing (Wang et al., 2011).

25   Simulation model, another alternative method, can obtain distribution, transboundary transport fluxes,

and major transport channel of Beijing in combination with meteorological data (An et al., 2012).

However, current studies mainly focus on ground-based observations, lacking stereoscopic monitoring

data that can help better understand the source and transport of air pollution.

Mobile DOAS provides another novel remote sensing method to obtain stereoscopic monitoring data

30   and characterize regional distribution of air pollution over medium- to large-distance scale. This

Atmospheric
Chemistry
and Physics
Discussions

technique can detect the horizontal distribution of pollutants with high spatial–temporal resolution and

rapidly identify the location of pollution sources. Furthermore, information on the upper layer of air

pollution can be investigated. Thus, transport of air pollution can be analyzed and associated with

meteorological trajectory data. At present, some related studies have been carried out (Ibrahim et al.,

5   2010; Shaiganfar et al., 2011). In China, several measurements are also performed in Shanghai and

Guangzhou. Wang et al. (2012) evaluated the NO_2 variation over the central urban area before and after

Shanghai Expo 2010 (Wang et al., 2012). Wu et al. (2013) observed the distribution and emission of

SO_2 and NO_2 in Guangzhou Eastern Area during Guangzhou Asian Games 2010(Wu et al., 2013).

However, this study is to summarize the distribution of SO_2 and NO_2, verify the type of air pollution

10   sources, and to discuss potential of transport from NCP to Beijing over NCP area. In addition, the

mobile platform referred in this study is also equipped with some point instruments from Peking

University (PKU) to synchronously measure near-surface concentration of gas and particulate mass.

In this paper, we present the observations of SO_2 and NO_2VCD in NCP from June to July 2013 using

mobile DOAS, and the distributions of SO_2 and NO_2 VCD in NCP are characterized. In combination

15   with ground surface data (point instrument), the characteristics of SO_2 and NO_2 along southwest and

southeast pathway under different wind fields are characterized and the hot spots and their possible

sources along the measurement paths are determined. The pollution transport pathways to Beijing are

revealed and first time convinced by capturing the plume. Finally, the NO_2 VCDs from mobile DOAS

data are compared with those from Ozone Monitoring Instrument (OMI). Obtained data are in good

20   agreement.

This paper is organized as follows: the experimental process, including overview of the measurements

and instruments. Wind fields and the principle of retrieval of vertical density of tropospheric trace gas

are discussed in detail in Sect. 2. Section 3 gives us the results and discussions, including distributions

of SO_2 and NO_2 tropospheric VCDs over NCP and analysis of hot spot and comparison with OMI NO_2.

25   Finally, the conclusions are presented in Sect. 4.

2. Experimental

2.1 Overview of the measurements

To characterize the spatial distributions of SO_2 and NO_2 VCD and investigate the potential transport to

30   Beijing, the measurement routes are specially designed. The entire measurement period from 11June to

16 July 2013 is initially divided into five identical cycles. Mobile DOAS observations span four cycles (from 11 June to 7 July) and cover four different routes because of bad weather or vehicle problem. Figure 1 depicts the detailed routes of mobile DOAS measurements. Cycle 1 covers five routes with a total path of 1400 km and takes five days to complete. The five routes are Beijing (BJ) to Shijiazhuang

5 (SJZ), Shijiazhuang to Dezhou (DZ), Dezhou to Baoding (BD) to Cangzhou (CZ), Cangzhou to Zhuozhou (ZZ), and Zhuozhou to Beijing for cycle1. Due to the bad weather or vehicle problem, Cycles 2 and 3 took four and three days to complete, resulting in skipping of some routes. We needed one more day to complete Cycle 4 due to power failure on 4 July. The details of monitoring information are listed in Table 1.

10 The approximate starting and ending times are 10:00 and 14:00 (Local Time, LT), particularly considering stable boundary layer and battery endurance. During the entire measurement period, the temperature varied from 30 ℃ to 36 ℃, and the wind fields were dominated by south and north.

2.2 Instrument description

Mobile DOAS instrument collects scattered sunlight from zenith observation. Details of the instrument

15 and performances are described in our previous study (Wu et al., 2013). Briefly, the system consists of telescope, a miniature fiber spectrometer unit, global positioning system, and computer. The series of Ocean Optics HR2000 is selected as miniature spectrometer, with spectral resolution of 0.6 nm and spectral range of 290 nm to 420 nm. The spectrometer is stored in a temperature-controlled unit to stabilize the temperature at +30±0.1 ℃ to avoid spectral shifts caused by temperature variations. The

20 detection limits of the instrument is approximately $3–5 \times 10^{15}$ molec./cm^2 for SO_2 and NO_2. The instrument is installed on an IVECO Turin V diesel vehicle (L = 6.6 m, W = 2.4 m, H = 2.8 m; payload = 2.7 metric tons), which is a mobile laboratory platform from PKU (Wang et al., 2009, 2011). The mobile DOAS system is powered by 220V alternating current through conversion of +12V direct current battery with a power converter.

25 In addition, PKU has set up some point instruments on the van, including SO_2 analyzer (ECOTECH 9850A), NO_x analyzer (ECOTECH 9841A), CO analyzer (ECOTECH 9830A), ozone analyzer (ECOTECH 9810A), and CO_2 analyzer (ECOTECH 9820A). Aside from gaseous pollutant instruments, some aerosol instruments, such as GRIMM and Dusttrak for $PM_{2.5}$ and Fast Mobility Particle Sizer, were also available onboard for analysis of particle size distribution. The details of the setup and

30 performance of the instruments are described in Wang et al. (2009, 2011).

2.3 Backward Lagrangian Trajectory Simulation

Apart from the near-surface wind data, the backward trajectory of air mass from the stations in Beijing

was also simulated using the Hybrid Single Particle Lagrangian Integrated Trajectory model (HYSPLIT,

offline version), which has been developed by the Air Resources Laboratory of the US National

5   Oceanic and Atmospheric Administration. An average boundary layer height (BLH) of around 1000m

has been calculated during noontime in summer over NCP area by Lv et al based on lidar observations.

The middle altitude of BLH, i.e., 500m, is taken as the representative horizontal transport height to

investigate transport effect on an assumption of well mixing throughout the whole BL around noontime.

So, backward trajectories were calculated once every 2 h for 1 day (24 h) at a selected altitude of 500 m

10   above ground level for each cycle. An archive meteorological database with a horizontal resolution of 1 °

$\times$ 1 ° from the Global Data Assimilation System, which is enough to identify the original regions of air

mass, is chosen to run the HYSPLIT model.

Figure 2 shows the cluster average backward trajectory for Cycles 1, 2, 3, and 4. During the

measurement periods of Cycles 1 and 3, all air masses came from the southern regions. For Cycle 2, the

15   mean back trajectory is roughly split equally between north and south. However, the dominant wind

field is north during the mobile DOAS observations for Cycle 2, except for the wind on 21 June as

listed in Table 1. A small different wind field is present for Cycle 4. The north wind account for nearly

72% and the south wind 28%. The detailed different observation periods of mobile DOAS exhibit that

dominant wind is south except for that on 2 and 5 July.

20   ### 2.4 Retrieval of Vertical Density of Tropospheric Trace Gas

SO_2 and NO_2 column densities are retrieved from zenith sky mobile DOAS with WinDOAS software.

Each measured spectrum starts with dark current, and offset corrections is divided through Fraunhofer

reference spectrum (FRS), which is a relative "clean-air" spectrum. One FRS spectrum is selected to

retrieve all other measured spectra during the whole field campaign. The FRS is recorded at

25   approximately 11:30 LT on April 30, 2013, near Bohai Sea, considering strong wind and good air

quality on that day (see Fig. 1a). After the retrieval procedures of logarithm of the ratio of measured

spectrum to FRS spectrum and high-pass and low-pass filtering, the differential slant column density

(DSCD), which is relative to the value of Frauenhofer spectrum, is obtained. A retrieval example of

SO_2 and NO_2 DSCD are illustrated in Fig. 3.

30   The wavelength range of SO_2 fit is 310 nm–324 nm and 338 nm–379 nm for NO_2 fit with WinDOAS.

Atmospheric
Chemistry
and Physics
Discussions

The high-resolution absorption cross-sections of SO_2, NO_2, HCHO, and O_3 at 293 K from Bogumil et al. (2003) are used in DOAS SO_2 fit. The NO_2 fit included the cross-section of NO_2, HCHO, and O_3 at 293K (Bogumil et al., 2003) and O_4 at 298 K (Greenblatt et al., 1990). In addition, the FRS and Ring spectrum are also included. The synthetic Ring spectrum is yielded from FRS spectrum using DOASIS

5　software (Kraus, 2006). The slit function is generated from the emission peak of mercury lamp at 334 nm. The high-resolution solar spectrum is used to calibrate wavelength. The fit uncertainties of NO_2 and SO_2 for the spectrum, as shown in Fig. 3, are approximately 2.48% and 1.84%. The typical uncertainties are less than 15% for NO_2 and 20% for SO_2.

The above obtained the DSCD with respect to FRS spectrum. Tropospheric NO_2 is $\sim 5 \times 10^{15}$ molec./cm^2

10　at the location of FRS spectrum on 30 April, 2013 from OMI result. Given the poor SO_2 satellite data, we checked the SO_2 results at ground level from a local environmental protection agency on that day. Compared with the high pollution over NCP area, we neglected these relatively small tropospheric contents in FRS spectrum. As a result, the tropospheric NO_2 and SO_2 VCD can be calculated with air mass factor (AMF) using the following formula:

15　$$VCD_{trop} = \frac{SCD_{trop}}{AMF_{trop}} = \frac{DSCD + SCD_{FRS} - SCD_{strat}}{DAMF + AMF_{FRS} - AMF_{strat}} = \frac{DSCD}{AMF_{trop}} \quad (1)$$

The radiative transfer model McArtim (Deutschmann et al., 2011) based on the Monte Carlo method is used to calculate the AMF_{trop}. We assume that aerosol and trace gas profiles are homogeneous below the BLH, whereas exponential profiles are above. Here, the constant concentrations within 1000m of boundary layer are assumed to be approximate 40 ppb and 10 ppb for NO_2 and SO_2 according to

20　state-controlled air-sampling sites. This hypothesis can lead to less than 5% uncertainty based on a sensitivity study by varying the setting of NO_2 and SO_2 setting. The average aerosol optical density (AOD) of 1.0 is estimated from the AERONET on June and July, 2013 at Xianghe site. The profiles of aerosol, NO_2, and SO_2 are taken from the LOWTRAN database and US standard atmosphere above the boundary layer. We estimate the total retrieval errors of NO_2 VCD and SO_2 VCD to be less than 20%

25　and 25% (Wu et al., 2013).

3.　**Results and discussion**

3.1　**Distributions of SO_2 and NO_2 Tropospheric VCDs over NCP**

In this section, the distributions of SO_2 and NO_2 tropospheric VCDs over NCP area are discussed with mobile DOAS observations. First, the overall distributions of SO_2 and NO_2 tropospheric VCDs along the measurement routes under the different dominant winds are characterized. Furthermore, we analyze the spatial and temporal variations of SO_2 and NO_2 tropospheric VCDs along the southwest routes

5 (Shijiazhuang–Baoding–Beijing) and southeast routes (Dezhou–Cangzhou–Tianjin–Beijing) for different wind fields. The possible transport route of trace gas is identified using these distribution characteristics.

3.1.1 Overall Distributions of SO_2 and NO_2 Tropospheric VCDs

Completing each cycle measurements takes four to five days, and this can lead to the probed air mass

10 change when meteorological condition varies rapidly. However, as described in Sect. 2.3 and listed in Table 1, the dominant wind field as a main influencing factor on air mass variation has not significantly changed, particularly the dominant wind direction of southerly and northerly winds during the measurement periods for mobile DOAS. However, air mass variation can also be affected by some other factors, such as temperature, humidity, and pressure, but the atmospheric physical reaction

15 processes is too complicated to discuss in this study. Thus, we assume that, in this work, the air mass does not change dramatically for each cycle measurements.

Typical spatial distributions of SO_2 and NO_2 along the measurement route over NCP area for north and south wind fields are shown in Fig. 4. The maps of SO_2 in Fig. 4 show that increased values are observed under the southerly wind, particularly the results along Taihang Mountain, which is also part

20 of the southwest measurement route (Shijiazhuang-Baoding-Beijing). The high SO_2 VCDs detected in the region near the cities of Shijiazhuang, Baoding, and Beijing indicate that these regions have emission sources of SO_2. In addition, high SO_2 VCDs are also observed on the cross-section of south route, particularly near Ji'nan City. This hot spot can always be found under the southerly wind during the field campaign, suggesting a strong emission outside the measurement area and south of it. Based

25 on the backward trajectory analysis, the big air pollution plume comes from Liaocheng City, which is another small city close to Ji'nan western region. Furthermore, relatively low SO_2 VCDs are observed along the southeast route compared with that of the southwest route.

However, for the northerly wind, no increased SO_2 VCDs are noted along the Taihang Mountain. The hot spot near Ji'nan City also disappeared. The downwind SO_2 VCDs of Shijiazhuang and Tianjin city

30 are relatively high due to source emission near the city. The results of comparison of wind direction

from south versus north further suggest that the strong emission sources located at the southern region of the measurement area have a significant influence on Beijing under the southerly wind, particularly along the Taihang Mountain.

Unlike SO_2, no significant difference between the southerly and northerly wind for NO_2 VCDs was

5   noted. The NO_2 VCDs are affected by the "city effect." High NO_2 VCDs are obtained near Beijing and Shijiazhuang City. The same is noted for SO_2, and due to strong emission source contribution, enhanced NO_2 VCDs are also found near Jinan City.

3.1.2 Spatial and temporal variations of SO_2 and NO_2 along southwest and southeast routes under different wind fields

10   As detailed in above analysis, the characteristics of SO_2 and NO_2 distributions have significant variations, including spatial and temporal differences along the southwest and southeast measurement routes. This section firstly investigates the SO_2 and NO_2 characteristics along southwest and southeast routes and then compares them with the results under southerly and northerly wind.

Table 2 lists the SO_2 and NO_2VCD from mobile DOAS and near-surface concentration from point

15   instrument under southerly and northerly wind along the southwest and southeast routes. For the southwest measurement route, the mean VCDs of SO_2 and NO_2 are 4.22×10^{16}molec./cm^2 and 1.69×10^{16}molec./cm^2. The mean near-surface concentration is 9.74 ppb and 111.28 ppb for SO_2 and NO_2. For the southeast measurement route, the mean VCDs of SO_2 and NO_2 are 3.40×10^{16}molec./cm^2 and 1.15×10^{16}molec./cm^2. The mean near-surface concentration of SO_2 and NO_2 is 17.27 ppb and 117.97 ppb.

20   The VCDs along southwest route are higher than that along the southeast route. However, the near-surface concentration along the different routes is reverse.

The vertical column and in situ measurements are discussed simultaneously in Table 2. It is interesting to note that such discussions can provide comprehensive information about surface emission and tropospheric pollution. We can also calculate the depth of a layer of air with the in situ mixing ratio and

25   the measured vertical column on the assumption of homogenous mixing within the planetary boundary layer (Chen et al., 2009). However, the height of the layer could not be estimated in this way in this study because the in situ measurements contaminated by very local vehicle emission, especially for NO_2. The traffic exhaust is one of the major contributors to NO_2 and large traffic emission result in the inhomogenous mixing within the planetary boundary layer, so it is found that the NO_2 layer would be

30   something like only 30 to 60m thick using above analysis method, which is very unreasonable

Atmospheric
Chemistry
and Physics
Discussions

compared to normal situations. In contrast, the SO_2 layer would vary from about 0.5 to 2.0 km thick, which is in the normal range.

The comparisons of VCDs between different wind fields show that the VCDs under southerly wind are much higher than that under northerly wind along the southwest route, particularly for SO_2, with the

5   value of 6.09×10^{16} molec./cm^2 and 2.35×10^{16} molec./cm^2. However, this phenomenon is not significant along the southeast route. In addition, the comparisons of SO_2 near-surface concentration suggest that the difference between the different wind fields is not significant along the southwest route, but is enhanced dramatically along the southeast route under southerly wind, with the value of 23.29 ppb versus 11.24 ppb under the northerly wind.

10   **3.1.3 Characterization of emission sources and identification of transport route**

Both results from mobile DOAS and point instruments observations for every measurement day are shown in Fig. 5 to Fig. 8. According to the "Box-Chart" plot, some distinct peak values of SO_2 VCDs are measured in the case of the south wind, whereas this is not significant for SO_2 near-surface concentration, as shown in Fig. 5. These findings indicate that the elevated sources existed along the

15   southwest measurement route, and the elevated sources are the main SO_2 sources along the southwest route. We could also infer that the high SO_2 value may be located in the upper layer. No significant peak values for NO_2 VCD (see Fig. 6) are noted. However, we found them on near-surface concentration, such as on 11 June. The results show that the traffic emission located at the near surface is the main sources of NO_2. If we traverse areas with large volumes of vehicles, the NO_2 near-surface

20   concentration should increase. However, for the southeast measurement routes, we did not observe the peak values of SO_2 VCDs and near-surface concentrations, as shown in Fig. 7. One interesting finding is that the SO_2 VCD on 21 June increased slightly from "Box-Chart" plot in Fig. 7. These findings verify that the low nonpoint sources are the main contributors along the southeast routes. However, the emissions of elevated sources from western part of the measurement region could account for the SO_2

25   peak value on 21 June (the dominant wind is west on that day), and this is in agreement with the results along southwest routes. As shown in Fig. 8, the NO_2 VCDs for south wind are 1.38 times higher than that for north wind, but the near-surface concentrations are almost equal for these two different winds. The same is true for SO_2; we also did not find elevated NO_2 sources along the southeast routes.

Based on the above analysis, we could infer that the pollution source along the southwest and southeast

30   routes have two types. The finding is also proven by the emission inventory: several large emission

sources are located southwestern region, and some near-surface fugitive sources are located

southeastern region (Wang et al., 2011).

Similar with SO_2, the average NO_2 VCD along the southeast route is lower than that along the

southwest route, but the near-surface concentration is higher than that along the southwest routes. The

5 near-surface vehicle emissions are the major contributors of NO_2, and fugitive emission sources are

additional sources of NO_2. In addition, the high NO_2 near-surface concentration along the southeast

route indicates large traffic volume over this region. This is also consistent with the fact that the

southeast route is an expressway from Beijing to Shanghai, the two most economically developed cities

in China. Additionally, trade exchanges among these two and other cities are frequent.

10 The VCDs and near-surface concentrations of SO_2 and NO_2 are high under the southerly wind in most

cases, particularly for SO_2 VCDs along the southwest routes and SO_2 near-surface concentrations along

the southeast routes. From mobile DOAS observations, the significant variations of SO_2 VCDs along

the southwest routes (also along Taihang Mountain) are shown in Fig. 9. The variations of SO_2 VCDs

for the different wind fields indicate that the southwest route is a transport route of SO_2 for Beijing.

15 When the air plume comes from the south, the air quality in Beijing deteriorates. Figure 10 shows the

mean SO_2 concentrations for when south or north wind is dominant in Beijing. The monitoring data in

seven state-controlled air-sampling sites demonstrate that the average SO_2 concentrations ranged from

8.22 ppb to 13.04 ppb for south wind and from 3.71 ppb to 5.02 ppb for north wind during the mobile

DOAS observation period in the Beijing area. Previous studies also confirmed the presence of this

20 transport route using other methods (Su et al., 2014). This work not only identifies the transport route

of SO_2 with mobile DOAS observations, but also determines the high SO_2 concentration existing in the

upper layer combination the concurrent near-surface data.

3.2 Analysis of hot spot

The hot spots are observed for the route of Shijiazhuang–Dezhou measurements under southerly wind.

25 The maximum SO_2 VCD and NO_2 VCD can reach 4.84×10^{17} molec./cm^2 and 7.41×10^{16} molec./cm^2.

However, the hot spots are not detected for the north wind. Figures 11 and 12 present the results of SO_2

and NO_2VCDs for the Shijiazhuang–Dezhou measurements under southerly and northerly wind.

Figure 11 exhibits a large polluted air mass coming from southern region in the rectangular area [Fig.

11 (a1) and Fig. 11(b1)] under southerly wind on 12 June. First, this air mass led to the rapid

30 enhancement of SO_2 and NO_2 VCDs in Area I and Location 1 [Fig.11 (a1), (a2), (b1), and (b2)]; then,

the VCDs in Area II and Location 2 increased subsequently due to the air mass diffusion. The time

series of SO_2 and NO_2 VCDs tell us that with the increase of distance, the peak value decreased in Area

II and observed width of air mass enlarged because of air mass diffusion. For Area I, the peak values of

SO_2 and NO_2 VCDs are 4.43×10^{17} molec./cm^2 and 6.80×10^{16} molec./cm^2 at 13:02 (LT). However, the

5   peak value for SO_2 and NO_2 decreased to 3.44×10^{17} molec./cm^2 and 4.68×10^{16} molec./cm^2 in Area II

at 13:43 (LT).

Furthermore, observed widths of air mass are estimated in Area I and Area II from the time series of

SO_2 VCDs in Fig. 10 (a3) using the following formula:

$$W = \sum_i (t_{i+1} - t_i) \cdot \overline{V}_{i+1 \to i} \quad (2),$$

10   where i is the number of spectrum in Fig. 11(a3), t_{i+1} and t_i are the time for the spectrum of i and

$i + 1$, and $\overline{V}_{i+1 \to i}$ is the mean car speed between t_{i+1} and t_i.

Using the above formula, the average observed width of air mass is calculated to be 11.83 km in Area I

and 17.23 km in Area II. Combined with the observed widths for Areas I and II and the geometric

relationships between these two locations, the distance of the air pollution sources from the Area I is

15   estimated at a distance of approximately 61.39 km. The distance of Area I from Liaocheng City is

approximately 60 km, proving that the source is indeed located in Liaocheng City, as discussed in Sect.

3.1.1.

While the above peak values are not found under the northerly wind as shown in Fig. 12, this

phenomenon further confirmed the large sources located at the southern region outside the

20   measurement area. When the dominant wind comes from south, the air quality of the measurement area

is severely influenced by the sources.

In addition, we simultaneously compare the one-minute average VCD results with the one-minute

near-surface concentrations along the Shijiazhuang–Dezhou routes. Figure 13 shows the time series of

VCDs and near-surface concentrations for SO_2 and NO_2 along the measurement route under the

25   southerly and northerly wind. For the specific southerly wind, such as on 3 July, the high SO_2 and NO_2

VCDs were captured through mobile DOAS in the areas, as shown in Fig. 11 (a2) or (b2) (the area

marked with sparse rectangular box in Fig. 13). This also indicates that the polluted air mass contained

high levels of SO_2 and NO_2. Furthermore, from the time series observations of SO_2 near-surface

concentrations, high near-surface concentrations are observed simultaneously in the sparse rectangle, as

Atmospheric
Chemistry
and Physics
Discussions
Open Access
EGU

shown in Fig. 13 (a), and this is the same as SO_2 VCDs. The combined results demonstrate that part of the air mass have deposited, resulting in the increase of SO_2 near-surface concentration. However, one interesting thing has been found the NO_2 near-surface concentration does not significantly increase in this area [Fig. 13 (b)]. Following the above explanation regarding SO_2, the declined air mass is

5 supposed to cause an increase in NO_2 near-surface concentration. The lifetime of NO_2 is less than SO_2, and the NO_2 conversion to other species, such as nitrate, could account for this unexpected finding. For the northerly wind, both VCDs and near-surface concentrations do not increase in the sparse box area. The correlation analysis between NO_2 and CO near-surface concentrations [Fig. 13 (e) and (f)] shows that NO_2 near-surface concentration mainly results from vehicle exhaust, regardless of the specific

10 wind direction.

3.3 Comparison with OMI NO_2

The OMI, which is onboard the Aura satellite of the Earth Observing System, was launched on 15 June 2004 with a nadir viewing mode (Levelt et al., 2006). OMI can be used to monitor global atmospheric NO_2 distribution with high spatial (up to 13×24 km) and temporal (daily global coverage) resolution.

15 OMI is equipped with two charge-coupled devices spanning a wavelength range from 264 nm to 504 nm to measure the solar scattering in the ultraviolet and visible spectra. The overpass time of OMI is 13:45 (LT) on the ascending node. In the current study, the OMI tropospheric NO_2 data product from NASA is used. The data consisted of three steps to derive tropospheric NO_2 VCD. The SCDs of NO_2 are derived from the OMI collected spectra based on the DOAS method in the wavelength ranging

20 from 405 nm to 465 nm. The air mass factors (AMFs) are applied to convert the SCDs to VCDs and are calculated with the monthly average NO_2 profile shapes (Rotman et al., 2001). Finally, the stratospheric contribution is estimated to derive tropospheric NO_2 VCDs by subtracting the stratospheric columns. Detailed description of tropospheric NO_2 retrieval process can be found in Bucsela et al. (2013).

In this study, to achieve a better comparison between OMI and mobile DOAS, the OMI tropospheric

25 NO_2 data are gridded onto a $0.1\,° \times 0.1\,°$ with an error and area weighted gridding algorithm (Wenig et al., 2008). The cloud fraction of 0.4 is used as a threshold to filter out the data with a cloud cover larger than 0.4. As a result, a total of 8 days (11, 12, 13, 18, 25, and 26 June and 3 and 6 July) of measurements from both OMI and mobile DOAS can be used for data comparison.

The comparisons of NO_2 VCDs between both datasets for our 8-day measurement are shown in Fig. 14.

30 The similar spatial pattern is captured by both OMI and mobile DOAS. In most cases, high level of

NO_2 VCD is observed around Shijiazhuang area. However, the hot spots of mobile DOAS observations, as shown in Sect. 3.2, cannot be detected completely using OMI due to the insensitivity of OMI observation to near-surface sources.

However, the NO_2 VCDs along southwest route are higher than that along the southeast route from

5   OMI observations, the same as discussed in Sect. 3.1.2. Moreover, the mobile DOAS data are averaged within each gridded satellite pixel (0.1 °×0.1 °) and compared to OMI values within each gridded pixel for every day of the 8-day measurement. And the correlation analysis for all the datasets of the 8-day measurement is shown in Fig. 15. The correlation coefficient (R^2) is 0.65, suggesting that both observations agree reasonably well. However, a systematic difference between the mobile DOAS and

10   OMI NO_2 VCDs is exist as shown in Fig. 15 implied by the fitted slope that is significantly less than unity (0.55). These discrepancies can be attributed to source emission from near surface (e.g. traffic exhaust, industrial sources etc.) or lower troposphere (e.g. elevated sources). The OMI observations are insensitivity to the local sources due to the limited spatial resolution and shield by aerosols and clouds. However, the mobile DOAS have an ability of rapid response to local sources, especially for lower

15   troposphere, like elevated sources. Also some studies have shown that the OMI NO_2 VCDs are systematically smaller than mobile DOAS and MAX-DOAS observations over polluted areas (Shaiganfar et al., 2011, Chan et al., 2015). Of course, some other factors can also result in these differences, like NO_2 diurnal cycle, different hypothesis on calculation of AMFs etc. The measurement time of mobile DOAS is approximately from 10:00 to 14:00, and the OMI overpass time may be 13:45.

20   Previous studies (Wu et al., 2013) have shown that the strong diurnal variations of NO_2 occur between 10:00 and 11:00. As a result, the time mismatch between OMI and NO_2 could result in different NO_2 VCDs. In addition, the NO_2 VCDs of OMI and mobile DOAS need to be converted from SCDs with AMFs. The calculations of AMFs should consider the trace gas profiles, aerosol profiles, ground albedo and wavelength etc. These different sets can yield different AMFs and VCDs.

25

4. Conclusions

The NCP has been experiencing severe air pollution associated with unprecedented economic boom and accelerated urbanization over the past few years. To characterize the temporal and spatial distribution and to investigate the effect of various sources on air quality, particularly for Beijing, the

30   observations of tropospheric SO_2 and NO_2 vertical column through mobile DOAS are performed from

Atmospheric
Chemistry
and Physics
Discussions

11 June to 7 July 2013.

Combined with the simultaneous measurement of ground surface concentration through point instruments, the various temporal and spatial distributions of SO_2 and NO_2 under different wind fields are discussed. For the southwest measurement route, the mean SO_2 VCD under southerly wind is 6.09

5 $\times 10^{16}$ molec./cm^2, which is 2.6 times higher than that for north wind (2.35×10^{16} molec./cm^2). The near-surface SO_2 concentration under southerly wind is 1.24 times higher than that under northerly wind, with the value of 10.78 ppb and 8.69ppb. Except for SO_2, the mean NO_2 VCD and near-surface NO_2 concentration under southerly wind are 1.77 and 1.42 times higher than that under northerly wind. The significant discrepancies of SO_2 VCD between the two various wind indicate that the transport

10 from southern NCP area strongly affects the air quality over northern NCP area (like Beijing). And the primary contributors to SO_2 along this measurement route are elevated emission sources, like power plant and steel company etc. using the interrelated analysis of VCD and in situ concentration. Moreover, the transport route of the path (Shijiazhuang-Baoding-Beijing) is identified.

However, for the southeast measurement route, we did not find a distinct difference of SO_2 VCD under

15 different wind fields, with the value of 3.29×10^{16} molec./cm^2 and 3.51×10^{16} molec./cm^2 for south and north wind. The mean near-surface concentration of SO_2 for southerly wind is nearly double than that of the value under northerly wind, with the concentration of 23.29 ppb and 11.24 ppb. The NO_2 VCDs and near-surface concentrations along the southeast route also do not have significant variations. Under south wind, the NO_2 VCD and near-surface concentration are 1.34×10^{16} molec./cm^2 and 119.12 ppb.

20 Under north wind, the NO_2 VCD and near-surface concentration are 9.68×10^{15} molec./cm^2 and 116.82 ppb. The higher SO_2 near-surface concentration along the southeast route indicates the low area sources are the primary contributors to SO_2 rather than elevated sources.

Analysis of hot spot shows that the average observed width of air mass is 11.83 km and 17.23 km associated with air mass diffusion. Another interesting finding is that the NO_2 near-surface

25 concentration did not significantly enhance for the area of air mass. The lifetime of NO_2 is less than that of SO_2 and NO_2 conversion to other species could account for this unexpected findings. The correlation analysis between NO_2 and CO near-surface concentrations shows that NO_2 near-surface concentration mainly resulted from vehicle exhaust regardless of specific wind direction.

Furthermore, comparison with OMI NO_2 VCDs indicates a reasonable agreement between OMI and

30 mobile DOAS with correlation coefficient (R^2) of 0.65. Both datasets have similar spatial patterns. In

most cases, the high level of NO$_2$ VCDs is observed around Shijiazhuang area. However, the fitted slop of 0.55 is significantly less than unity may reflect the existence of some near surface local sources which are insensitive observations or underestimation by OMI. This study will promote the development and extend mobile DOAS technique to rapidly capture the regional distribution of air

5   pollutants and evaluate the potential transport as well as the use of satellite validation.

References

15   An, J. L.，Li, J., Zhang, W., Chen, Y., Qu, Y., Xiang, W. L.: Simulation of transboundary transport fluxes of air pollutants among Beijing，Tianjin，and Hebei Province of China, Acta Scientiae Circumstantiae，32(11) : 2684-2692, 2012.

Boichu, M., Clarisse, L., Péré, J.-C., Herbin, H., Goloub, P., Thieuleux, F., Ducos, F., Clerbaux, C., and Tanré, D.: Temporal variations of flux and altitude of sulfur dioxide emissions during volcanic

20   eruptions: implications for long-range dispersal of volcanic clouds, Atmos. Chem. Phys., 15, 8381–8400, 2015

Bucsela, E.J., Krotkov, N.A., Celarier, E.A., Lamsal, L.N., Swartz, W.H., Bhartia, P.K., Boersma, K.F., Veefkind, J.P., Gleason, J.F., Pickering, K.E.: A new stratospheric and tropospheric NO2 retrieval algorithm for nadir-viewing satellite instruments: applications to OMI. Atmos. Meas. Tech. 6 (10),

25   2607e2626, 2013

Bogumil, K., Orphal, J., Homann, T., Voigt, S., Spietz, P., Fleischmann, O. C., Vogel, A., Hartmann,M., Kromminga, H., Bovensmann, H., Frerick, J., and Burrows, J. P.: Measurements of molecular absorption spectra with the SCIAMACHY preflight model: instrument characterization and reference data for atmospheric remote-sensing in the 230–2380 nm region, J. Photoch. Photobio.

30   A, 157, 167–184, 2003.

Chen, D., Zhou, B., Beirle, S., Chen, L. M. and Wagner, T.: Tropospheric NO_2 column densities deduced from zenith-sky DOAS measurements in Shanghai, China, and their application to satellite validation, Atmos. Chem. Phys., 9, 3641–3662, 2009.

Chan, K. L, Hartl, A., Lam, Y. F., Xie, P. H., Liu, W. Q., Cheung, H. M., Lampel, J., Pohlerf, D., Li, A., Xu, J., Zhou, H. J., Ning, Z., Wenig, M. O.: Observations of tropospheric NO_2 using ground based MAX-DOAS and OMI measurements during the Shanghai World Expo 2010, Atmos. Environ., 119, 45-58, 2015.

Crutzen, P. J.,: The influence of nitrogen oxides on the atmospheric ozone content. Q. J. R. Meteorol. Soc. 96 (408), 320-325, 1970

Deutschmann, T., Beirle, S., Frieß U., Grzegorski, M., Kern, C., Kritten, L., Platt, U., Prados-Roman, C., Pukite, J., Wagner, T., Werner, B., Pfeilsticker, K.: The Monte Carlo atmospheric radiative transfer model McArtim: Introduction and validation of Jacobians and 3D features, Journal of Quantitative Spectroscopy & Radiative Transfer, 112, 1119–1137, 2011.

Finlayson-Pitts, B. J. and Pitts, J. N.: Chemistry of the Upper and Lower Atmosphere: Theory, Experiments, and Applications, Academic Press, San Diego, USA, 1999.

Guo, S., Hu, M., Misti L, Z., Peng, J., Shang, D., Zheng, J., Du, Z., Wu, Z., Shao, M., Zeng, L., Mario J, M., and Zhang, R.: Elucidating severe urban haze formation in China, PNAS, 111,17373–17378, 2014.

Greenblatt, G. D., Orlando, J. J., Burkholder, J. B., and Ravishankara, A. R.: Absorption measurements of oxygen between 330 nm and 1140 nm, J. Geophys. Res.-Atmos., 95, 18577–18582, doi:10.1029/JD095iD11p18577, 1990.

Huang, R., Zhang, Y., Bozzetti, C., Kin-Fai, H., Cao, J., Han, Y., Daellenbach, K. R., Slowik, J. G., Platt, S. M., Canonaco, F., Zotter, P., RobertWolf, Simone, M. P., Emily, A. B., Monica C., Giancarlo, C., Andrea, P., Margit, S., Gulcin, A., Jurgen, S. K., Ralf, Z., Zhisheng, A., Sonke, S., Urs, B., Imad, E. H., Andre S. H. Prevot: High secondary aerosol contribution to particulate pollution during haze events in China, Nature, 514, 218-222, 2014.

Hu, J. L., Wang, Y. G., Ying, Q., Zhang, H. L.: Spatial and temporal variability of $PM_{2.5}$ and PM_{10} over the North China Plain and the Yangtze River Delta, China, Atmos. Environ., 95, 598-609, 2014

Ibrahim, O., Shaiganfar, R., Sinreich, R., Stein, T., Platt, U., and Wagner, T.: Car MAX-DOAS measurements around entire cities: quantification of NOx emissions from the cities of Mannheim

Atmospheric
Chemistry
and Physics
Discussions

and Ludwigshafen (Germany), Atmos. Meas. Tech., 3, 709–721, doi:10.5194/amt-3-709-2010, 2010.

Lv, L. H., Liu, W. Q., Zhang, T. S., Dong, Y. S., Chen, Z. Y., Fan, G. Q., Liu, Y., Xiang, Y.: Characteristics of Boundary Layer Height in Jing-Jin-Ji Area Based on Lidar, Laser & Optoelectronics Progress, 54, 010101-1~7, 2017. (in Chinese)

Ji, D. S., Li, L., Wang, Y., Zhang, J., Cheng, M., Sun, Y., Liu, Z., Wang, L. L., Tang, G. Q.,, Hua, B., Chao, N., Wen, T., Miao, H.: The heaviest particulate air-pollution episodes occurred in northern China in January, 2013: Insights gained from observation, Atmos. Environ., 92, 546-556, 2014

Jang, M., Kamens, R.M.: Characterization of secondary aerosol from the photooxidation of toluene in the presence of NOx and 1-propene. Environ. Sci. Technol. 35 (18), 3626-3639, 2001

Kanaya, Y., Irie, H., Takashima, H., Iwabuchi, H., Akimoto, H., Sudo, K., Gu, M., Chong, J., Kim, Y. J., Lee, H., Li, A., Si, F., Xu, J., Xie, P. H., Liu, W. Q., Dzhola, A., Postylyakov, O., Ivanov, V., Grechko, E., Terpugova, S., and Panchenko, M.: Long-term MAX-DOAS network observations of NO_2 in Russia and Asia (MADRAS) during the period 2007–2012: instrumentation, elucidation of climatology, and comparisons with OMI satellite observations and global model simulations, Atmos. Chem. Phys., 14, 7909-7927, doi:10.5194/acp-14-7909-2014, 2014.

Kraus, S.: DOASIS, A Framework Design for DOAS, PhD-thesis, University of Mannheim, Shaker Verlag, Heidelberg, Germany, 2006.

Lee, H. L., Kim, Y. J., Jung, J., Lee, C., Klaus-Peter, H., Platt, U., Hu, M., Zhu, T.: Spatial and temporal variations in NO_2 distributions over Beijing, China measured by imaging differential optical absorption spectroscopy, Journal of Environmental Management, 90, 1814–1823, 2009

Levelt, P. F., van den Oord, G. H. J., and Dobber, M. R.: The ozone monitoring instrument, IEEE T. Geosci. Remote, 44, 1093–1101, 2006.

Ma, J. Z., Wang, W., Chen, Y., Liu, H. J., Yan, P., Ding, G. A., Wang, M. L., Sun, J., and Lelieveld, J.: The IPAC-NC field campaign: a pollution and oxidization pool in the lower atmosphere over Huabei, China, Atmos. Chem. Phys., 12, 3883–3908, 2012

Matsui, H., Koike, M., Kondo, Y., Takegawa, N., Kita, K., Miyazaki, Y., Hu, M., Chang, S.-Y., Blake, D. R., Fast, J. D., Zaveri, R. A., Streets, D. G., Zhang, Q., and Zhu, T., Spatial and temporal variations of aerosols around Beijing in summer 2006: Model evaluation and source apportionment, J. Geophys. Res., 114, D00G13, doi:10.1029/2008JD010906, 2009.

Atmospheric
Chemistry
and Physics
Discussions

Quan, J., Zhang, Q., He, H., Liu, J., Huang, M., and Jin H.,: Analysis of the formation of fog and haze in North China Plain (NCP), Atmos. Chem. Phys., 11, 8205−8214, 2011

Ramanathan, V. and Crutzen, P. J.: New directions: Atmospheric brown "Clouds", Atmos. Environ., 37, 4033–4035, 2003.

5   Rotman, D.A., Tannahill, J.R., Kinnison, D. E., Connell, P. S., Bergmann, D., Proctor, D., Rodriguez, J. M., Lin, S. J., Rood, R. B., Prather, M.J., Rasch, P.J., Considine, D.B., Ramaroson, R., Kawa, S. R.: Global modeling initiative assessment model: model description, integration, and testing of the transport shell. J. Geophys. Res. Atmos. 106 (D2), 1669e1691, 2001

Su, F. Q., Gao, Q. X., Zhang, Z. G., Ren, Z. H., Yang, X. X.: Transport Pathways of Pollutants from

10   Outside in Atmosphere Boundary Layer, Research of Environmental Sciences, 17,1: 26-30, 2014. (in Chinese)

Sun, Y., Q. Jiang, Z. Wang, P. Fu, J. Li, T. Yang, and Y. Yin: Investigation of the sources and evolution processes of severe haze pollution in Beijing in January 2013, J. Geophys. Res. Atmos.,119, 4380–4398, doi: 10.1002/2014JD021641, 2014

15   Sun, Y. L., Wang, Z. F., Fu P. Q., Yang T., Jiang, Q., Dong, H. B., Li, J., and Jia, J. J.: Aerosol composition, sources and processes during wintertime in Beijing, China, Atmos. Chem. Phys., 13, 4577–4592, 2013

Shaiganfar, R., Beirle, S., Sharma, M., Chauhan, A., Singh, R. P., and Wagner, T.: Estimation of NOx emissions from Delhi using Car MAX-DOAS observations and comparison with OMI satellite

20   data, Atmos. Chem. Phys., 11, 10871−10887,doi:10.5194/acp-11-10871-2011, 2011.

van Donkelaar, A., Martin, R.V., Brauer, M., Kahn, R., Levy, R., Verduzco, C., Villeneuve, P.J. Global estimates of ambient Fine particulate matter concentrations from satellite-based aerosol optical depth: development and application. Environ. Health Perspect. 118, 847-855, 2010.

Wang, Y. S., Yao, L., Wang, L. L., Liu, Z. R., Ji, D. S., Tang, G. Q., Zhang, J. K., Sun, Y., Hu, B., Xin, J.

25   Y.: Mechanism for the formation of the January 2013 heavy haze pollution episode over central and eastern China. Science China: Earth Sciences, 57: 14−25, doi: 10.1007/s11430-013-4773-4, 2014a

Wang, Z. F., Li, J., Wang, Z., Yang, W. Y., Tang, X., Ge, B. Z., Yan, P. Z., Zhu, L. L., Chen, X. S., Chen, H. S., Wang, W., Li, J. J., Liu, B., Wang, X. Y., Wang, W., Zhao, Y. L., Lu, N., Su, D. B.: Modeling

30   study of regional severe hazes over mid-eastern China in January 2013 and its implications on

Atmospheric
Chemistry
and Physics
Discussions

pollution prevention and control, Science China: Earth Sciences, 57: 3–13, doi:
10.1007/s11430-013-4793-0, 2014b

Wu, F. C., Xie, P. H., Li, A., Chan, K. L., Hartl, A., Wang, Y., Si, F. Q., Zeng, Y., Qin, M., Xu, J., Liu, J. G., Liu, W. Q., and Wenig, M: Observations of SO_2 and NO_2 by mobile DOAS in the Guangzhou eastern area during the Asian Games 2010, Atmos. Meas. Tech., 6, 2277–2292, 2013.

Wu, Q. Z., Wang, Z. F., Gbaguidi, A., Gao, C., Li, L. N., and Wang, W.: A numerical study of contributions to air pollution in Beijing during CAREBeijing-2006, Atmos. Chem. Phys., 11, 5997–6011, 2011.

Wang, S., Zhou, B., Wang, Z., Yang, S., Hao, N., Valks, P., Trautmann, T., and Chen, L.: Remote sensing of NO_2 emission from the central urban area of Shanghai (China) using the mobile DOAS technique, J. Geophys. Res., 117, D13305, doi:10.1029/2011JD016983, 2012.

Wang, M., Zhu, T., Zhang, J. P., Zhang, Q. H., Lin, W. W., Li, Y., Wang, Z. F.: Using a mobile laboratory to characterize the distribution and transport of sulfur dioxide in and around Beijing, Atmos. Chem. Phys., 11, 11631–11645, 2011

Wang, M., Zhu, T., Zheng, J., Zhang, R. Y., Zhang, S. Q., Xie, X. X., Han, Y. Q., and Li, Y.: Use of a mobile laboratory to evaluate changes in on-road air pollutants during the Beijing 2008 Summer Olympics , Atmos. Chem. Phys., 9, 8247–8263, 2009

Wenig, M. O., Cede, A. M., Bucsela, E. J., Celarier, E. A., Boersma, K. F., Veefkind, J. P., Brinksma, E. J., Gleason, J. F., and Herman, J. R.: Validation of OMI tropospheric NO_2 column densities using direct-sun mode Brewer measurements at NASA Goddard Space Flight Center, J. Geophys. Res., 133, D16S45, doi:10.1029/2007JD008988, 2008.

World Health Organization: WHO Air quality guidelines for particulate matter, ozone, nitrogen dioxide and sulfur dioxide Global update 2005 summary of risk assessment, Geneva, Switzerland, 2006.

Xu, J., Ma, J. Z., Zhang,   X. L., Xu, X. B., Xu, X. F., Lin, W. L., Wang, Y., Meng, W., and Ma, Z. Q.: Measurements of ozone and its precursors in Beijing during summertime: impact of urban plumes on ozone pollution in downwind rural areas, Atmos. Chem. Phys., 11, 12241–12252, 2011.

Xu, X. P., Wang, L. H., and Niu, T. H.: Air pollution and its health effects in beijing, Ecosyst. Health, 4, 199–209, 1998.

Ying Qi, Wu Li, Zhang Hongliang: Local and inter-regional contributions to PM2.5 nitrate and sulfate in China, Atmos. Environ., 94, 582-592, 2014

Yang, F., Tan, J., Zhao, Q., Du, Z., He, K., Ma, Y., Duan, F., Chen, G., and Zhao, Q.: Characteristics of PM2.5 speciation in representative megacities and across China, Atmos. Chem. Phys., 11, 5207–5219, 2011

Zhang, W., Zhu, T., Yang, W., Bai, Z., Sun, Y. L., Xu, Y., Yin, B., and Zhao, X.: Airborne measurements of gas and particle pollutants during CAREBeijing-2008, Atmos. Chem. Phys., 14, 301–316, 2014

Zhao, B., Wang, S. X., Wang, J. D., Fu, J. S., Liu, T. H., Xu, J. Y., Fu, X., Hao, J.: Impact of national NOx and SO_2 control policies on particulate matter pollution in China, Atmos. Environ., 77, 453-463, 2013a

Zhao, X. J., Zhao, P. S., Xu, J., Meng, W., Pu, W. W., Dong, F., He, D., and Shi, Q. F.: Analysis of a winter regional haze event and its formation mechanism in the North China Plain, Atmos. Chem. Phys., 13, 5685–5696, 2013b

Zhang, R., Jing, J., Tao, J., Hsu, S. C., Wang, G., Cao, J., Lee, C. S. L., Zhu, L., Chen, Z., Zhao, Y., and Shen, Z.: Chemical characterization and source apportionment of $PM_{2.5}$ in Beijing: seasonal perspective, Atmos. Chem. Phys., 13, 7053–7074, 2013

Atmospheric
Chemistry
and Physics
Discussions

Table 1 Summary of monitoring information of mobile DOAS. Wind data from airport meteorological data

http://www.wunderground.com

Cycles	Date	Time(LT)	Routes	Wind Direction	Wind Speed (m/s)
Cycle 1	11 June	10:14-14:00	BJ-SJZ	BJ: southeast	BJ: 2~3
				SJZ: southwest	SJZ: 1~2
	12 June	10:24-14:05	SJZ-DZ	SJZ: southwest	SJZ: 1~2
				DZ: southwest	DZ: 3~4
	13 June	10:20-15:04	DZ-BD-CZ	DZ: southwest	DZ: 4~5
				BD: south	BD: 2~3
				CZ: southwest	CZ: 4~5
	14 June	10:02-13:45	CZ-ZZ	CZ: southwest	CZ: 4~5
				ZZ: southwest	ZZ: 4~5
	15 June	09:57-14:06	ZZ-BJ	ZZ: south	ZZ: 2~3
				BJ: south	BJ: 2
Cycle 2	17 June	10:36-14:19	BJ-SJZ	BJ: northeast	BJ: 2~3
				SJZ: northeast	SJZ: 3
	18 June	10:02-13:32	SJZ-DZ	SJZ: north	SJZ: 1~2
				DZ: north	DZ: 1~2
	20 June	10:25-15:05	DZ-BD-CZ	DZ: northwest	DZ: 2~3
				BD: northwest	BD: 2~3
				CZ: northeast	CZ: 3~4
	21 June	09:57-13:24	CZ-ZZ	CZ: west	CZ: 3~4
				ZZ: southwest	ZZ: 2~3
Cycle 3	24 June	10:47-14:06	BJ-SJZ	BJ: southeast	BJ: 2~3
				SJZ: south	SJZ: 2~3
	25 June	10:10-14:17	SJZ-DZ	SJZ: south	SJZ: 1~2
				DZ: south	DZ: 3~4
	26 June	09:43-14:01	DZ-BJ	DZ: southwest	DZ: 4~5
				BJ: south	BJ: 3~4
Cycle 4	2 July	10:24-14:13	BJ-SJZ	BJ: northwest	BJ: 5~6
				SJZ: northwest	SJZ: 3~4
	3 July	10:26-14:01	SJZ-DZ	SJZ: southwest	SJZ: 2
				DZ: southwest	DZ: 3~4
	4 July	10:12-11:54	DZ-CZ	DZ: southwest	DZ: 3~4
				CZ: southeast	CZ: 1~2
	5 July	09:55-13:40	CZ-BD-CZ	CZ: northeast	CZ: 3~4
				BD: northeast	BD: 3~4
	6 July	09:56-14:23	CZ-ZZ	CZ: southeast	CZ: 2~3
				ZZ: southwest	ZZ: 2~3
	7 July	10:12-13:21	ZZ-BJ	ZZ: southeast	ZZ: 2~3
				BJ: southeast	BJ: 2~3

Atmospheric
Chemistry
and Physics
Discussions

Table 2 Both results measured through mobile DOAS and point instruments along the southwest and southeast

routes for different wind fields.

VCD [molec./cm^2]		South Wind	North Wind	Ratio	Average
Southwest Route	SO$_2$	6.09×10^{16}	2.35×10^{16}	2.69	4.22×10^{16}
	NO$_2$	2.16×10^{16}	1.22×10^{16}	1.77	1.69×10^{16}
Southeast Route	SO$_2$	3.29×10^{16}	3.51×10^{16}	0.94	3.40×10^{16}
	NO$_2$	1.34×10^{16}	9.68×10^{15}	1.38	1.15×10^{16}

Near surface Concentration [ppb]		South Wind	North Wind	Ratio	Average
Southwest Route	SO$_2$	10.78	8.69	1.24	9.74
	NO$_2$	130.55	92	1.42	111.28
Southeast Route	SO$_2$	23.29	11.24	2.07	17.27
	NO$_2$	119.12	116.82	1.02	117.97

*Ratio: defined as the value under southerly wind/northerly wind

5

Atmospheric
Chemistry
and Physics
Discussions
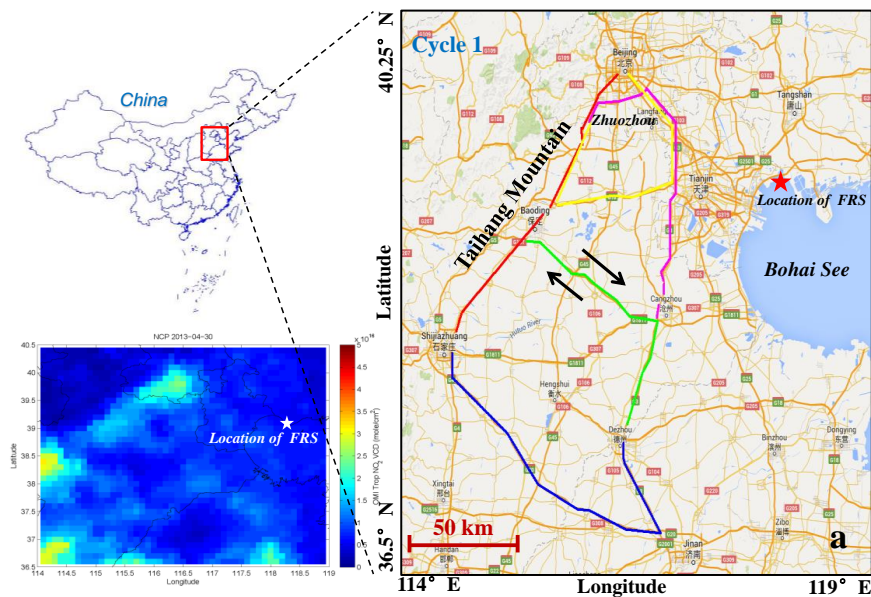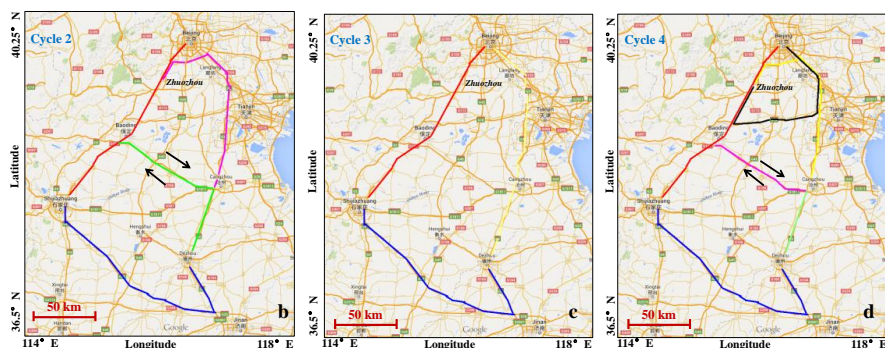
Figure 1: Maps of the mobile measurement areas and routes. The red, blue, green, pink, and yellow tracks show the

routes of BJ–SJZ, SJZ–DZ, DZ–BD–CZ, CZ–ZZ, and ZZ–BJ (a). The OMI NO$_2$ VCD on 30 April shows the NO$_2$

VCD of FRS is low (a). (a) also marks the location of FRS, Bohai See, and Taihang Mountain. The red, blue, green,

and pink tracks indicate the routes of BJ–SJZ, SJZ–DZ, DZ–BD–CZ, and CZ–ZZ (b). The red, blue, and yellow

tracks show the routes of BJ–SJZ, SJZ–DZ, and DZ–BJ (c). The red, blue, green, pink, yellow, and black tracks

show the routes of BJ–SJZ, SJZ–DZ, DZ–CZ, CZ–BD–CZ, CZ–ZZ, and ZZ–BJ (d). The black arrows indicate the

monitoring route from CZ to BD and return to CZ.
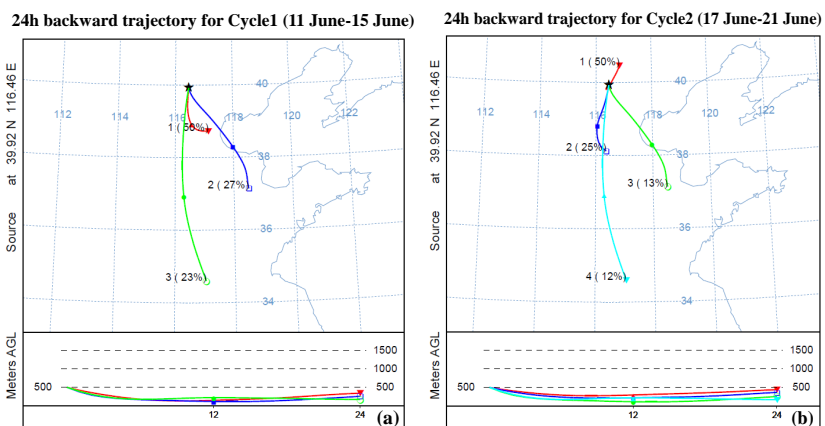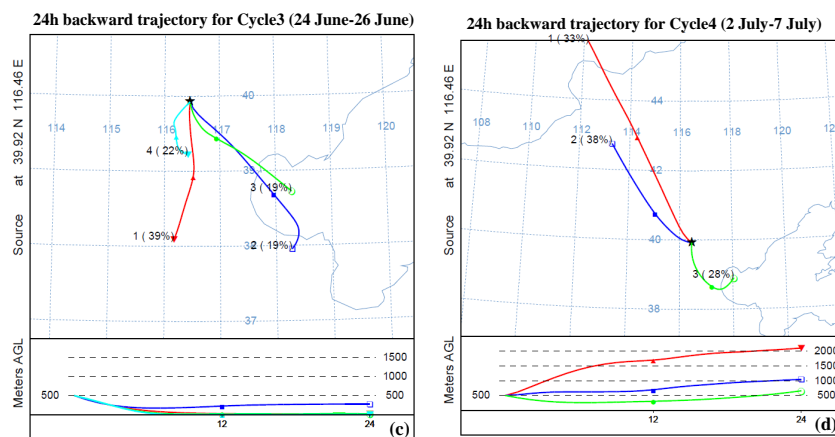
Figure 2: 24 h cluster mean air mass backward trajectories at 500 m height at Beijing for four different cycles. The black star shows the location of Beijing. The different color lines indicate air mass from different regions. (a), (b), (c), and (d) show the backward trajectory for Cycles 1, 2, 3, and 4, respectively. The percentages suggest the ratios of air mass in one region.
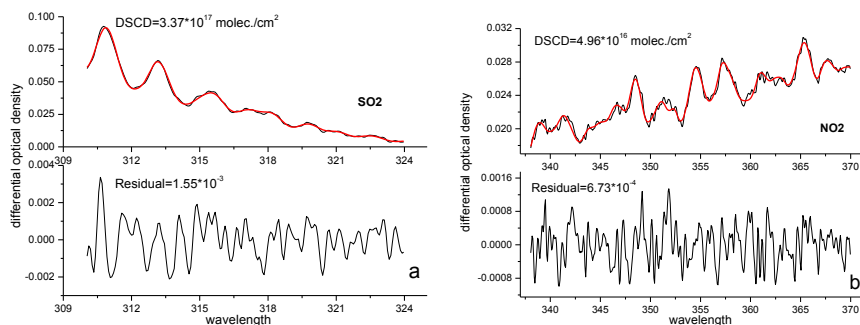
Figure 3: Example of SO_2 (a) and NO_2 (b) DSCD fit recorded at 13:04 (LT) on 12 June 2013. Black lines denote the differential optical densities (DODs) of measured spectrum, and red lines show the fit results. The DSCD is the SCD (Slant Column Density) with respect to FRS spectrum.
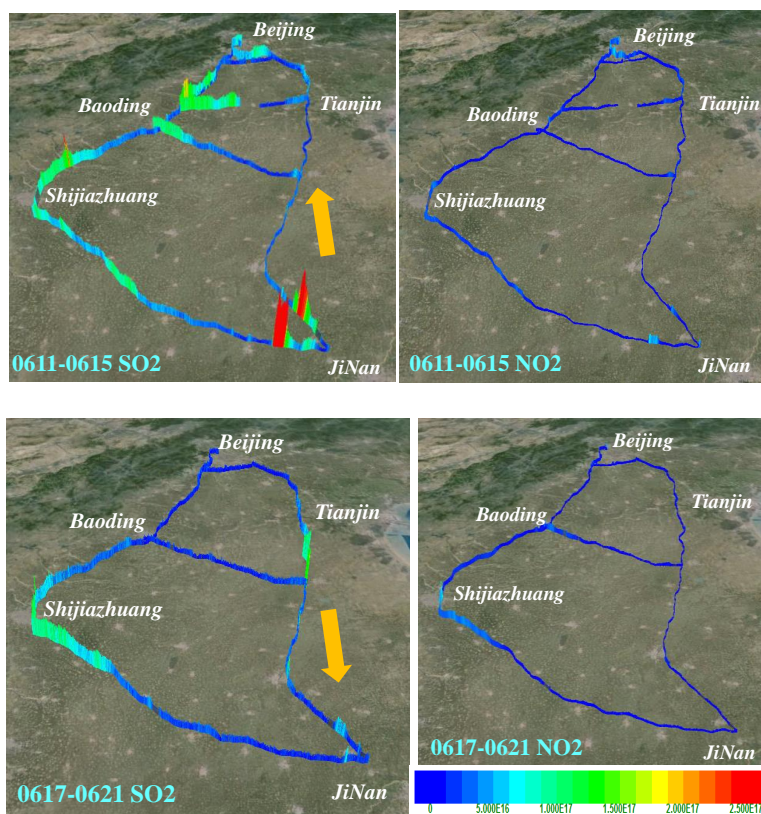
Figure 4: Spatial distributions of SO_2 and NO_2 VCDs over NCP area for north (17−21 June) and south (11−15 June)

wind fields; the orange arrows show the dominant wind direction.

5
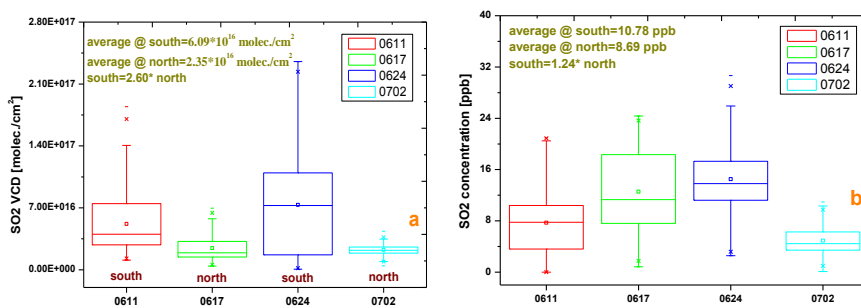
Figure 5: The SO_2 VCDs (a) and near-surface concentrations (b) along the southwest route.
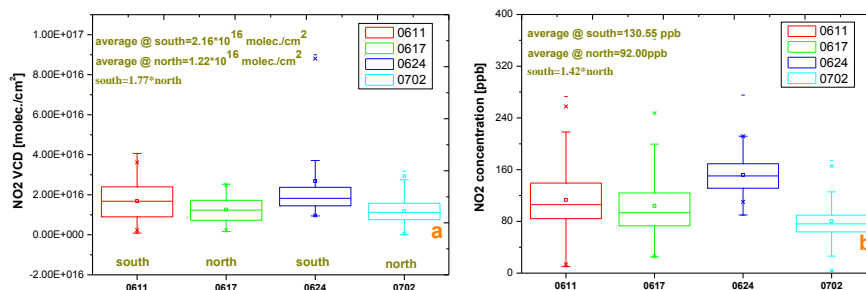
Figure 6: The NO$_2$ VCDs (a) and near-surface concentrations (b) along the southwest route.
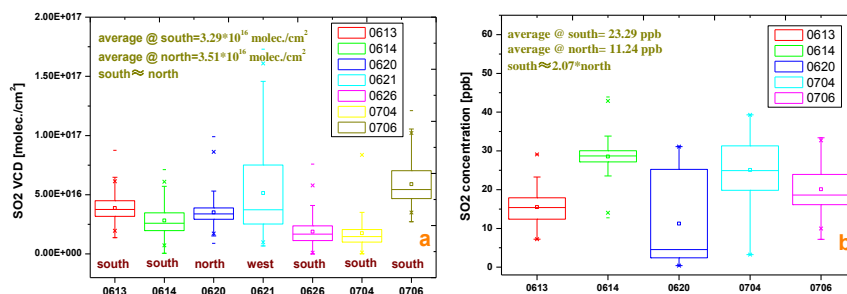
Figure 7: The SO$_2$ VCDs (a) and near-surface concentrations (b) along the southeast route; lack of near-surface

data on 21 June and 26 June due to instrument problems.
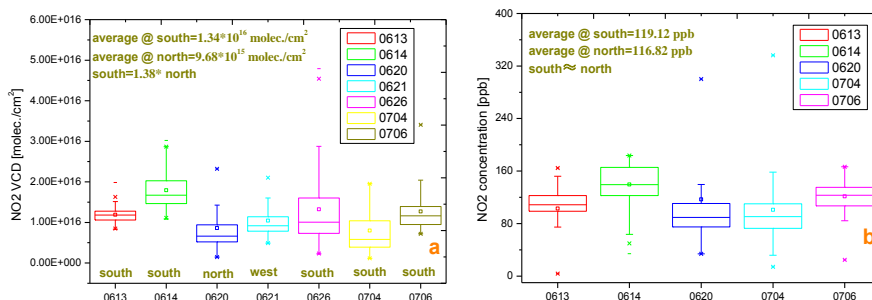
Figure 8: The NO$_2$ VCDs (a) and near-surface concentrations (b) along the southeast route; lack of near-surface

data on 21 June and 26 June due to instrument problems.

27
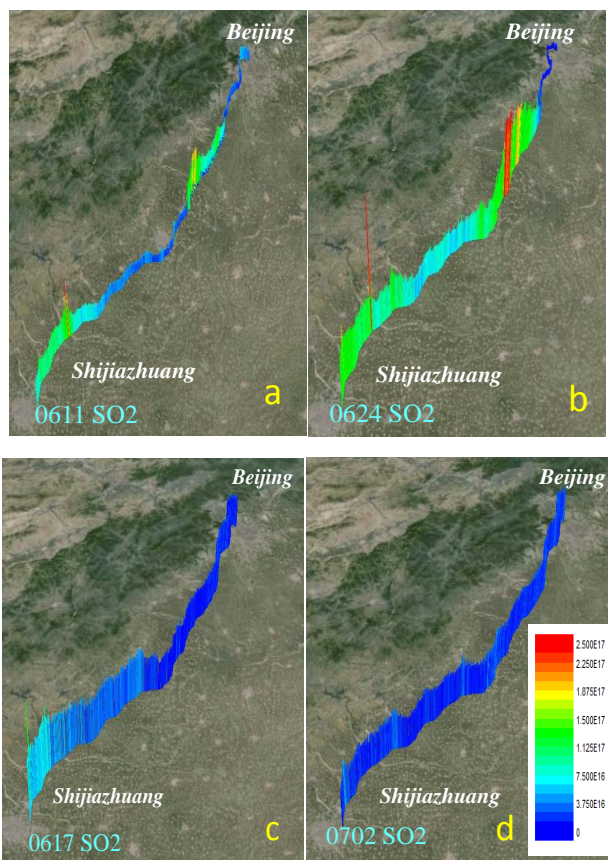
Figure 9: The variations of SO$_2$ VCDs along the southwest measurement routes (Beijing–Shijiazhuang) for south

(a and b) and north (c and d) wind fields.

5
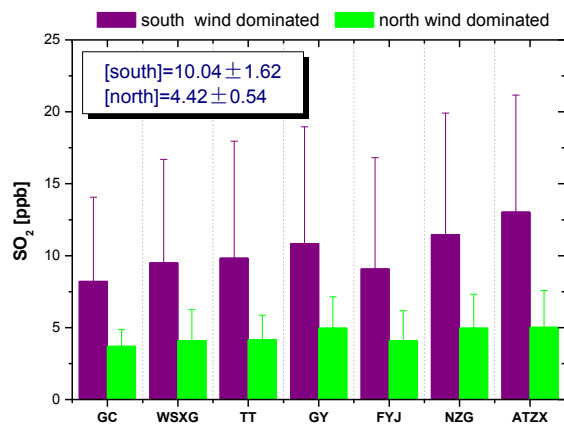
Figure 10: The mean concentrations of SO$_2$ measured at Gucheng (GC), Wanshou Xigong (GSXG), Tian Tan (TT),

Guangyuan (GY), Fuyoujie (FYJ), Nongzhanguan (NZG), and AoTiZhongxin (ATZX) sites based on the south

wind and north wind dominance in Beijing during mobile DOAS observations period. The bars show the standard

deviations of SO_2 concentrations.
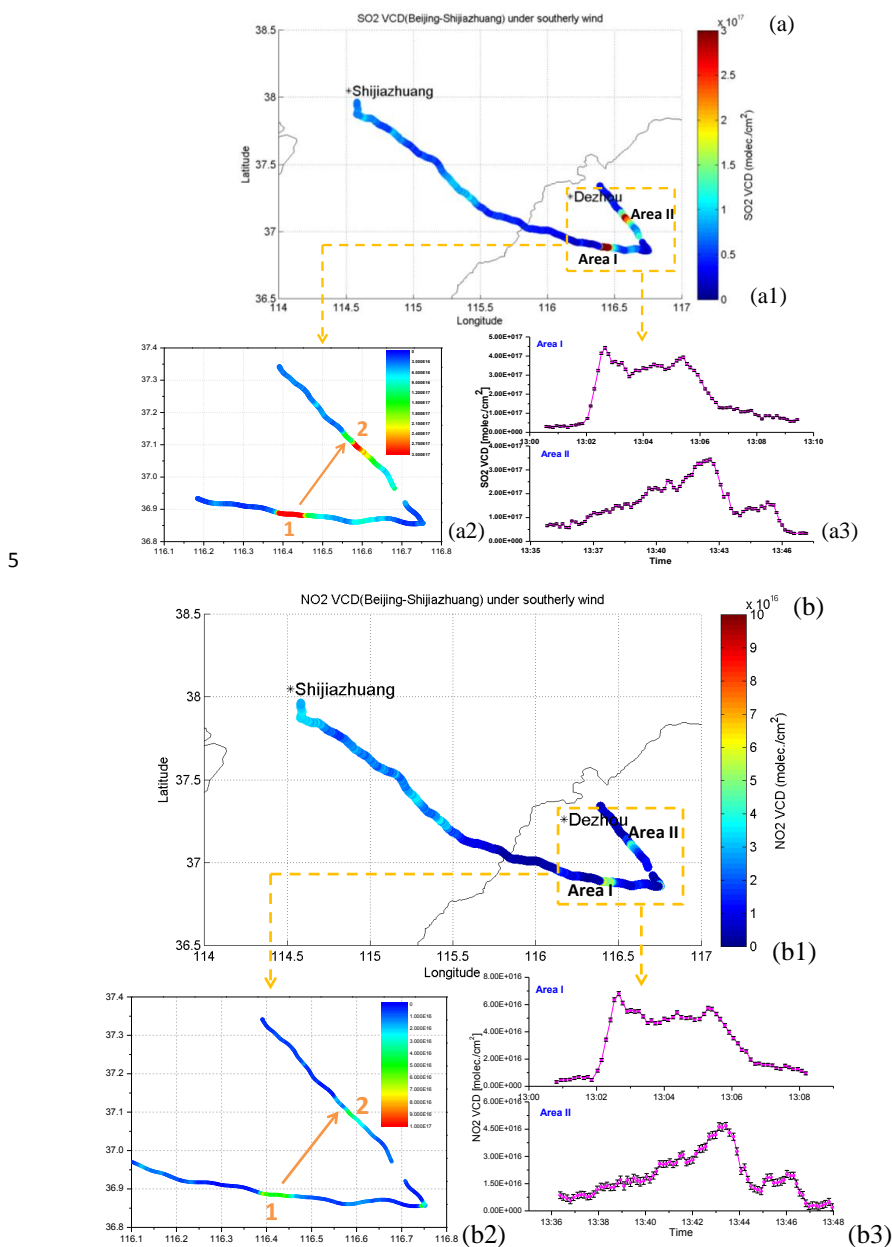
Figure 11: The hot spots of SO_2 (a) and NO_2 VCDs (b) are observed for the measurement of Shijiazhuang–Dezhou

City under southerly wind on 12 June. (a1): Distribution of SO_2 VCDs along the whole measurement route; (a2)

Distribution of SO_2 VCDs on hot spot area, where the origin arrow shows the diffusion of air mass from location 1

to location 2; (a3) time series of SO_2 VCDs for the polluted air mass for the rectangular area as shown in (a1),

5   where the top figure of (a3) shows the Area I and the bottom for the Area II. (b1), (b2), and (b3) are similar as (a1),

(a2), and (a3), only for NO_2.
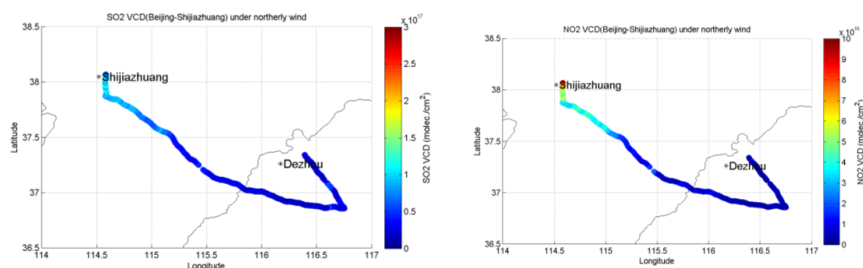
Figure 12: The distributions of SO_2 and NO_2 VCDs along the Shijiazhuang–Dezhou measurement route for
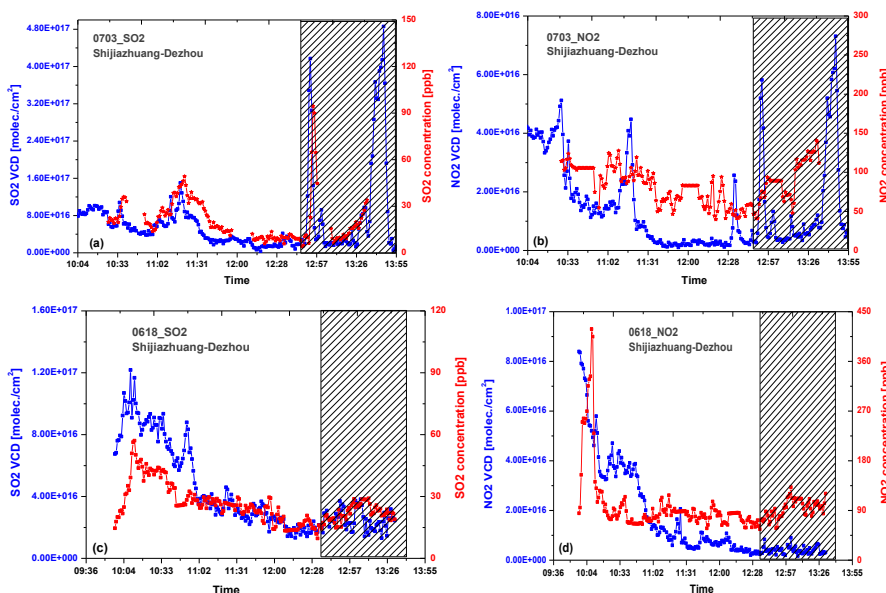
10   northerly wind.
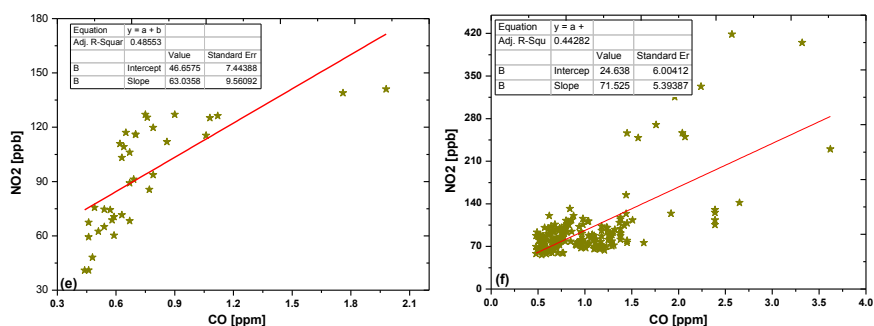
Figure 13: Time series of VCDs and near-surface concentrations of SO$_2$ and NO$_2$ along the route of Shijiazhuang–

Dezhou for south and north wind (a) and (b): SO$_2$ and NO$_2$ VCDs and near-surface concentrations on 3 July under

southerly wind; (c) and (d): SO$_2$ and NO$_2$ VCDs and near-surface concentrations on 18 June under northerly wind;

5   (e): correlation analysis between NO$_2$ and CO near-surface concentrations for south wind (3 July) for the sparse

rectangle area; (f) correlation analysis between NO$_2$ and CO near-surface concentrations for north wind (18 June)

for the sparse rectangle area. The sparse rectangular boxes show polluted air mass area as shown in Fig. 11.
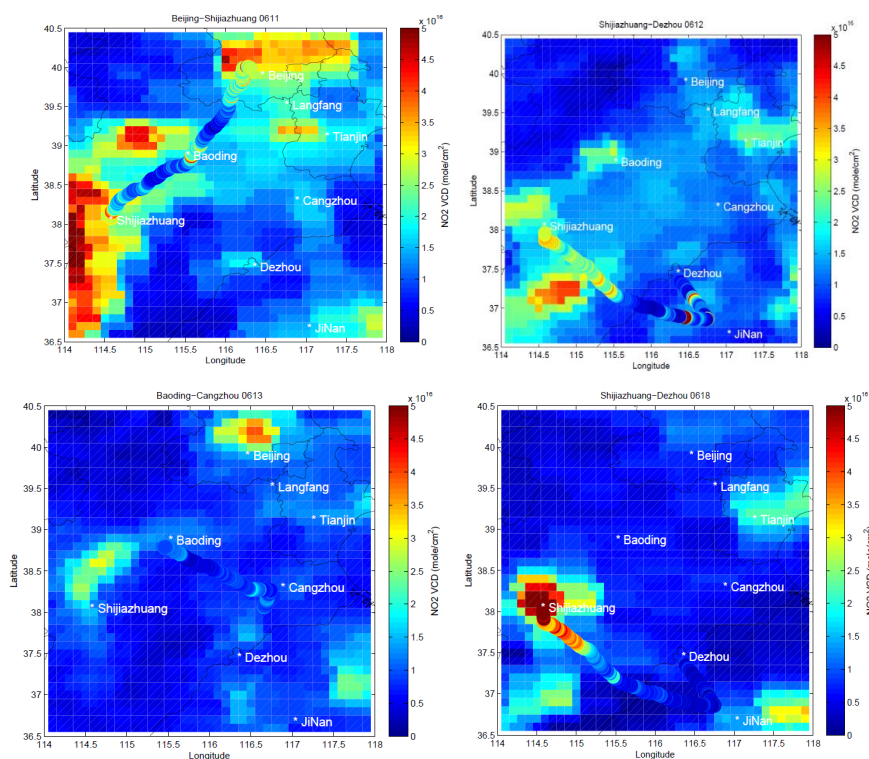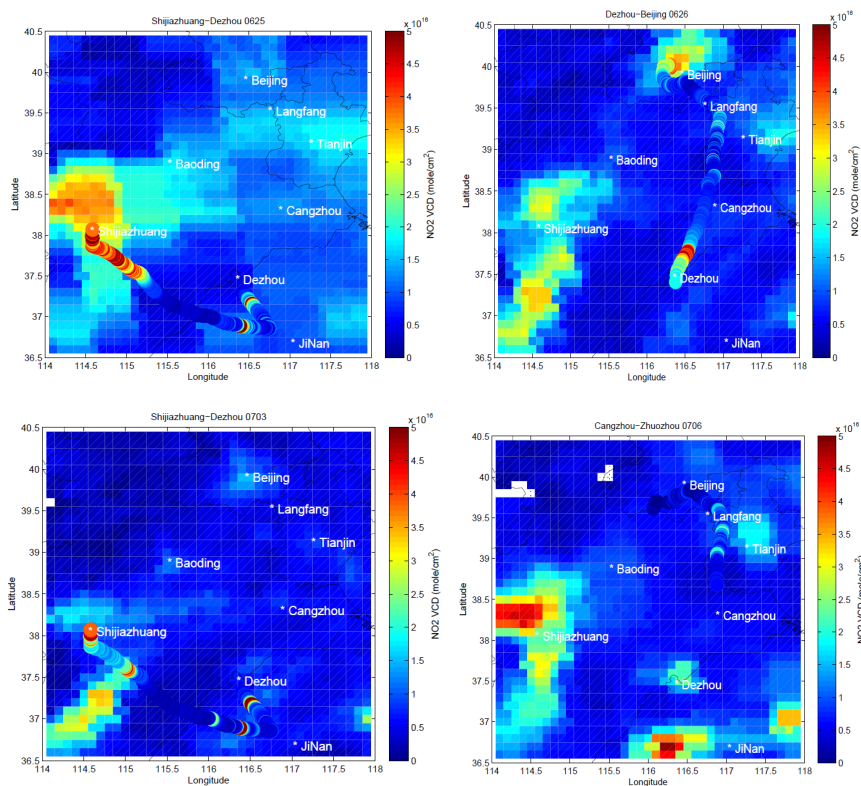

10

Figure 14: Spatial pattern of NO$_2$ measured through mobile DOAS and OMI. The header of each plot indicates measured route and date, such as the first plot showing the result of "Beijing–Shijiazhuang" route on 11 June. The color-coded circle indicates the mobile DOAS observations. The grid resolution of OMI was 0.1 °×0.1 °.
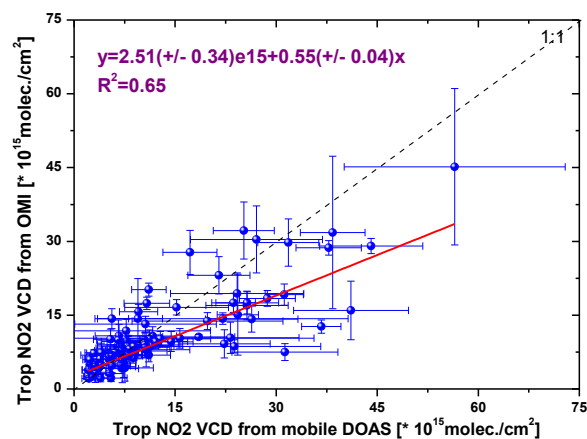

Figure 15: Correlation analysis of mobile DOAS and OMI NO$_2$ VCDs.